HEFAT2014
10th International Conference on Heat Transfer, Fluid Mechanics and Thermodynamics
14 - 16 July 2014
Orlando, Florida

ENHANCEMENT OF RAY TRACING METHOD FOR RADIATIVE HEAT TRANSFER WITH NEW ISOCELL QUASI-MONTE CARLO TECHNIQUE AND APPLICATION TO EUI SPACE INSTRUMENT

Jacques L.* and Masset L. and Kerschen G.
*Author for correspondence
Department of Aerospace and Mechanical Engineering,
Space Structures and Systems Laboratory
University of Liège,
Belgium,
E-mail: ljacques@ulg.ac.be

ABSTRACT

This paper presents the developments of the new isocell quasi-Monte Carlo ray tracing method for thermal analysis. The rationale for this research is the speed-up of radiative heat transfer computation with the Finite Element Method, widely used in mechanical engineering especially for space structure design but not yet often for thermal analysis of these structures.

Based on Nusselt's analogy, the ray direction sampling is done by sampling the unit disc to derive the ray directions. Stratified sampling is applied to the unit disc that is divided into cells or *strata* into which random points are generated. The isocell method relies on cells that have the particularity of presenting almost the same area and shape. This enhances the uniformity of the generated quasi-random sequence of ray directions and leads to faster convergence. The isocell method is associated with different surface sampling to derive REFs. The method is benchmarked against ESARAD, the standard ray tracing engine of the thermal analysis software used in the European aerospace industry. Various geometries are used. In particular, one entrance baffle of the Extreme Ultraviolet Imager (EUI) instrument developed at the Centre Spatial de Liège in Belgium is presented. The EUI instrument of the Solar Orbiter European Space Agency mission and will be launched in a 0.28 perihelion orbit around the Sun in 2018.

INTRODUCTION

The Finite Element Method (FEM) is widely used in mechanical engineering, in particular for space structure design but not yet often for thermal engineering of space structures where the finite difference method (lumped parameter or network-type method) is still dominant [1, 2]. However, present thermal analysis software too frequently involve awkwardness and error-prone manual input because of the lack of interaction with CAD and FE models and quite deficient pre- and post-processing user interfaces [2–6]. Despite this, the reason why FEM is not generally used is twofold: first because the radiation couplings computation, which are necessary for radiative heat transfer, is extremely expensive, and second due to their lack of flexibility to simulate custom specific operations (e.g. thermal control components such as heaters, heat-pipes,...) [4]. The second reason is mainly an implementation issue and would probably not involve any major difficulty. The present paper focuses on the first and main reason.

Mathematical models of thermal systems involving non-negligible radiative heat exchanges require the computation of the radiative exchange factors (REFs). Able to deal with realistic surface properties, the most general and efficient method to compute REFs is Monte Carlo ray tracing [7–9].

NOMENCLATURE

F_{ij}	[-]	View Factor between surface i and surface j
B_{ij}	[-]	Radiative Exchange Factor between surface i and surface j
θ	[rad]	polar angle
ϕ	[rad]	azimuthal angle
$\mathbf{r}$	[-]	ray direction
A	[m^2]	Surface area
Δ_B	[-]	RMS error on the REFs
Δ_T	[K]	RMS error on the temperatures
N_d	[-]	Number of directions
N_o	[-]	Number of origins
N_{rays}	[-]	Total number of rays
N_f	[-]	Number of faces

Combined with FEM, this method becomes however very computationally expensive due to the large number elements composing a FE model and the large number of rays to be fired to have meaningful REF results. Furthermore, REFs between finite element external facets involve handling huge non-sparse matrices which is again computationally demanding. Two approaches can be considered to alleviate these problems: reduce the number of rays fired from each face for a given accuracy and confidence level and/or decrease the number of faces by grouping the FE external facets into *super-faces*. This paper focuses on the first approach and presents the developments of the isocell method aiming at accelerating the convergence and increasing the accuracy of the ray tracing.

MONTE CARLO RAY TRACING

To compute REFs in complex geometries, classical analytical and numerical quadrature methods become rapidly inefficient if not impossible. On the contrary, the complexity of Monte Carlo methods increases linearly with the size and complexity of the problem. They are therefore well suited to the REF computation. Monte Carlo applied to ray tracing consists in tracing the history of statistically meaningful samples of photons (or photon bundles called rays) from their point of emission to their final absorption.

Monte Carlo methods were introduced in nuclear engineering during the 1940s and were first used for solving thermal radiation problem in the early 1960s by Fleck [10] and Howell [11, 12]. In the aerospace industry, the Monte Carlo ray tracing (MCRT) method was introduced in the 1970s with the NEVADA code [2]. Nowadays, it is part of most of the realistic radiative heat transfer software.

Monte Carlo ray tracing can be used to compute the view factors but it also offers the advantage to enable the direct computation of the radiative exchange factors, taking into account multiple reflections/transmissions and real surface properties, without adding too much complexity.

If N_i rays (or photon bundles) are emitted from the surface i among which N_{ij} rays are absorbed by surface j either directly or after any type/number of reflections/transmissions, the radiative exchange factor B_{ij} between surface i and surface j can be written:

$$B_{ij} = \lim_{N_i \to \infty} \frac{N_{ij}}{N_i} \cong \left. \frac{N_{ij}}{N_i} \right|_{N_i >> 1} \tag{1}$$

The view factor F_{ij} is obtained similarly by considering only direct absorption without any reflection or transmission of any kind. The basic concept of Monte Carlo method is that the number of rays must be large enough to be statistically meaningful so that the REF tends towards the correct answer. As any stochastic method, the results will vary randomly around the correct answer and the amplitude of the fluctuations decreases as the number of samples increases. Typical Monte Carlo convergence process is shown in Figure 1. The random samples are generated with pseudo-random generators, whose sequences are usually initialized with a seed. One given seed generates a determined sequence of pseudo-random numbers.

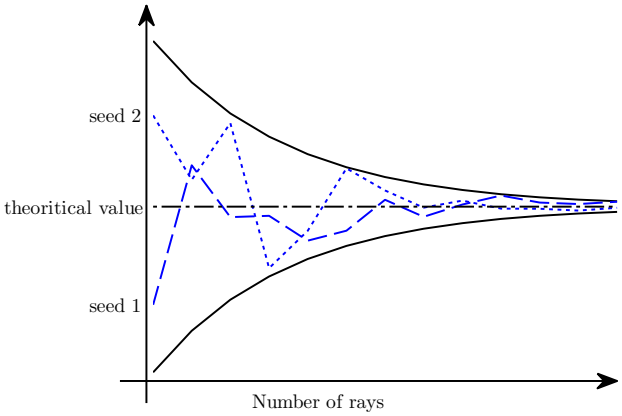

Figure 1 Typical Monte Carlo ray tracing process convergence.

The inconvenient of crude Monte Carlo techniques is their relatively low convergence rate: the error being inversely proportional to the square root of the number of rays [13–16]:

$$\text{error} \propto \frac{1}{\sqrt{N_{\text{rays}}}} \tag{2}$$

To compute the exchange factors between one surface and the surrounding surfaces, the rays must be distributed both over the directions and over the emitting surface area, in the same way that the view factor computation involves a double integration, first over the absorbing surface A_j then over the emitting surface A_i:

$$F_{ij} = \frac{1}{A_i} \int_{A_i} \int_{A_j} \frac{\cos\theta_i \cos\theta_j}{\pi r_{ij}^2} \chi_{ij} dA_j dA_i \tag{3}$$

χ_{ij} is the line-of-sight factor (1 if the two surfaces are mutually visible and 0 otherwise) and r_{ij} the distance between dA_i and dA_j.

Two separate samplings need to be performed: the direction sampling of the unit hemisphere and the spatial sampling of the emitting surface. Direction sampling of the unit hemisphere leads to the pointwise view factor which is then integrated over the emitting surface with the surface sampling. The isocell method focuses on the development of an alternative direction sampling scheme aiming at increasing the convergence rate and accuracy of the ray tracing process. The effect of several spatial sampling schemes will also be analysed.

ISOCELL DIRECTION SAMPLING

Random distribution

The basic and most common ray emission direction sampling is based on the cosine emission law (Lambert's cosine law [17]) for perfectly diffuse surface. In that case, the polar angle θ and azimuthal angle ϕ can be derived from two pseudo-random numbers R_θ and R_ϕ in $[0,1]$ through Equation 4 [9, 15].

$$\theta = \arcsin\sqrt{R_\theta} \qquad \phi = 2\pi R_\phi \tag{4}$$

For each pair of pseudo-random number (R_θ, R_ϕ), the ray direction is simply given by Equation 5.

$$r(\theta,\phi) = [\sin\theta\cos\phi \quad \sin\theta\sin\phi \quad \cos\theta]^\intercal \tag{5}$$

Based on Nusselt's analogy [18], Malley [19] proposed an equivalent method to generate the ray directions by sampling the unit disc. Nusselt's analogy states that the pointwise view factor between a point P on surface i and a surface j is equal to the area of its orthographic projection[1] divided by π (ratio of the projected area to the area of the unit disc). After sampling the unit disc with uniformly distributed pseudo-random numbers, each point on the unit disc defines a direction by projecting it back to the unit hemisphere. Figure 2 depicts Nusselt's analogy and Malley's method. With this method, the ray directions are obtained through Equation 6 where ϕ is given by the Equation 4 and r is a random variable uniformly distributed in $[0,1]$. Equation 6 is equivalent to 5 since $r = \sin\theta$.

$$r(r,\phi) = \left[r\cos\phi \quad r\sin\phi \quad \sqrt{1-r^2}\right]^\intercal \tag{6}$$

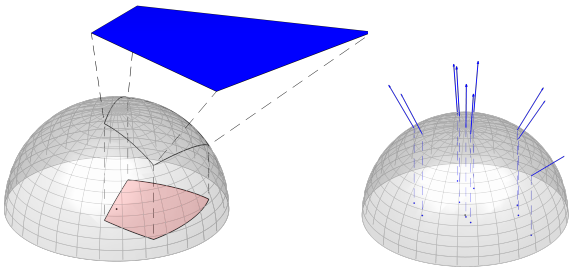

Figure 2 Nusselt's analogy with orthographic projection (left) and Malley's method (right).

It is worth noting that the hemi-cube method [20] also derives from Nusselt's analogy but presents some disadvantages recalled in [21].

Low-discrepancy sequences

One way to increase the accuracy and convergence rate of the ray tracing is to use quasi-Monte Carlo methods [13, 22]. Instead of being based on a sequence of pseudo-random numbers, the quasi-Monte Carlo method relies on low-discrepancy sequences. Such sequences offer the advantage of better uniformity over the integration domain. The Sobol sequence has already been used in reverse Monte Carlo ray tracing problems [23] and proved to be efficient. Another low-discrepancy sequence used in quasi-Monte Carlo simulations is the Halton sequence [24].

[1]The orthographic projection is composed of a projection on the unit sphere centered on point P and an orthogonal projection onto the plane of tangent to the surface i and point P

Stratified sampling

Another way to enhance the uniformity of the distribution over the hemisphere is to use stratified sampling [13, 22, 25]. Stratified sampling is another type of quasi-Monte Carlo method and consists in dividing the integration domain into *strata* that are randomly sampled independently. In [21], stratified sampling is applied to the hemisphere (referred as stratified hemisphere method) by dividing it along its parallels and meridians. To do so, the unit disc is divided into concentric rings of equal area and therefore corresponding to equal elementary view factors (from Nusselt's analogy). Each ring is then divided in equal sectors, based on meridians.

This particular stratified sampling leads to a better convergence rate τ (defined in Equation 7) of the view factor computation (0.75 instead of 0.5 for crude Monte Carlo).

$$\text{error} \propto N_{\text{rays}}^{-\tau} \tag{7}$$

Masset *et al.* showed in [26] that because the cells of the unit disc in this method have very different shapes (although they have the same area), the method behaves poorly in some particular configurations. This is the origin for the development of the isocell method to generate *strata* with more uniform aspect ratio.

Stratified sampling: isocell method

The need for a division of the unit disc into cells having both similar area and shape (aspect ratio) led to the development of the isocell method [27]. The method and properties of the cells are described in details in [26] and briefly recalled here. After being divided into n equally spaced rings as it was done in the stratified hemisphere method described above, each ring is not divided in the same number of cells anymore but in a number of cells increasing linearly with the ring radius.

If n is the number of rings and N_1 the number of cells dividing the initial central ring (actually a disc), the total number of cells is given by Equation 8:

$$N_{\text{cells}} = N_1 \sum_{i=1}^{n} (2i-1) = N_1 n^2 \tag{8}$$

It was shown in [26] that the cell shape factor β defined as the ratio between the square of the cell perimeter and its area was minimum for $N_1 = 3$: $\beta|_{N_1=3} = 16.01$ (16 for a square and 4π for a disc). Compared to [26], one random point within each cell instead of taking the center of the cell. This technique is called jittering [28] and is used to avoid potential aliasing.

Figure 3 compares the different unit disc sampling strategies. Stratified sampling schemes (based on isocell and the one from [21] based on meridians and parallels) and Halton sequence all give visually better results than crude random. Stratified sampling based on meridians and parallels ([21]) however shows some concentration of the points near the centre of the unit disc.

To assess the uniformity of the different unit disc sampling methods, the Voronoi tessellation corresponding to the sample

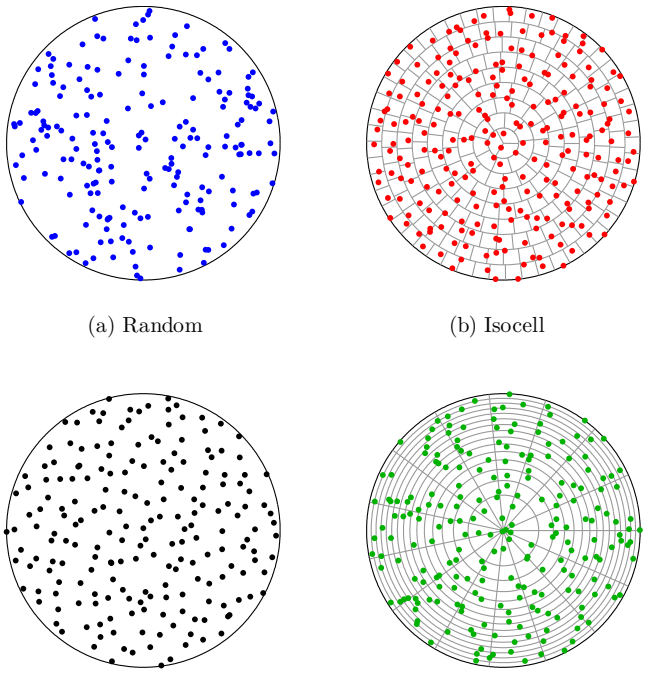

(a) Random (b) Isocell

(c) Halton sequence (d) Stratified hemisphere

Figure 3 Unit disc sampling with ≈ 200 origins with the different sampling schemes: random, isocell, stratified hemisphere and Halton sequence.

points is computed for each method. The distribution of the relative Voronoi cells area[2] is analysed. Figure 4 shows the distribution for the four sampling methods, using 10^4 sample points. To reduce the variations due to the randomness of the process, each curve results from the average of 100 runs. It confirms the results visually observed in Figure 3. The random sampling leads to a standard deviation of the relative Voronoi cells area of 0.53 that is twice as much as the isocell (0.25), Halton (0.23) distributions. The stratified hemisphere lies in between with a standard deviation of 0.33.

Application of isocell direction sampling to pointwise view factor computation

As mentioned before, the sampling of the unit disc (and hemisphere *via* Malley's method) is used to generate the pseudo or quasi-random ray directions. This direction set can be used directly with Equation 1 to compute the pointwise view factor by checking if the ray intersects the given face.

The pointwise view factor with a rectangle is computed with the different sampling techniques presented above and compared to the analytical solution [9]. Figure 5 shows the results and each data point corresponds to the average of 500 runs with its associated standard deviation. The solution obtained with the ray tracing engine of the European Space Agency thermal analysis software

[2] Voronoi cell area multiplied by the number of origins and divided by the area of the unit disc, π

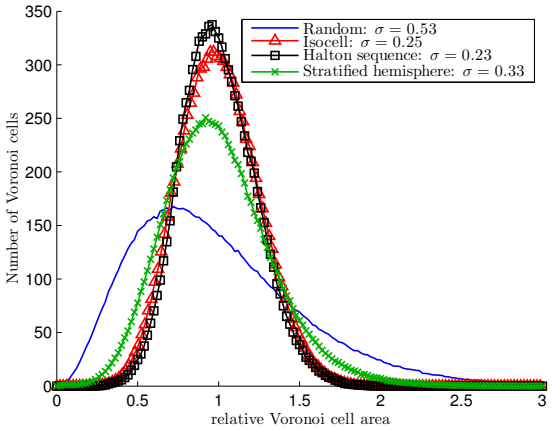

Figure 4 Typical distribution of the relative Voronoi cells area associated with the sampling of the unit disc (10^4 samples) for random, isocell, stratified hemisphere and Halton sequence sampling.

ESARAD [29] is also plotted. As presented in [15], ESARAD is based on a crude Monte Carlo ray tracing process and gives identical results to crude MCRT re-implemented in Matlab®. All three other quasi-MCRT techniques present lower mean error and better convergence rate. As expected, the convergence rate of crude Monte Carlo method tends to 0.5 while the quasi-MCRT schemes converge faster (rate approaching 0.75). The non-smooth behaviour of the stratified hemisphere method is explained by the poor uniformity of the sampling near the pole of the hemisphere, as explained above and in [26]. A convergence rate of 0.75 involves that each time the number of rays is multiplied by 2, the mean error is divided by 1.7 as opposed to 1.4 with a 0.5 convergence rate.

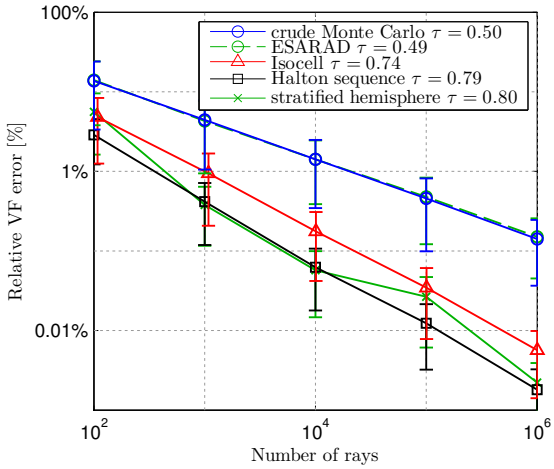

Figure 5 Evolution of the error of the point to rectangle view factor in function of the number of rays for the different sampling schemes. Error bars give the average and corresponding standard deviation based on 500 runs.

SURFACE SAMPLING

In the previous section, direction sampling was analysed and the pointwise view factor computed. To compute radiative heat transfer between finite surfaces, the integration over the emitting surface has to be performed. Again, numerical integration can be done by sampling the emitting surface. Different schemes are investigated and compared: random (*i.e.* pseudo-random) sampling, quasi-random sampling, uniform sampling, Gauss points sampling with associated weights (Gauss-Legendre quadrature rule).

For a total number of rays N_{rays} fired from a surface, N_d directions and N_o surface sampling points (origins) must be generated. The number of rays (directions) per origin is noted $N_{d/o}$. If the number of origins is the same as the number of directions, one ray (one direction) is fired from each origin and $N_{d/o} = 1$, $N_{\text{rays}} = N_d = N_o N_{d/o}$. A global direction sampling is thus performed and each ray direction is associated to one origin.

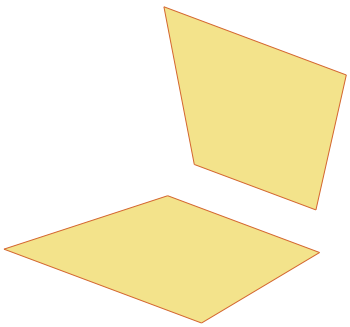

Figure 6 Representation of the geometry used for the benchmarking with perpendicular quadrangles.

If multiple rays are fired from each origin ($N_{d/o} > 1$), either local direction sampling is performed at each origin or a global direction sampling is distributed among the origins. The different strategies are tested and compared in the case of the radiative exchange factor between the two quadrangles in perpendicular planes shown in Figure 6. Each quadrangles is a single surface over which the spatial sample points (origins) are generated. In this example, the emittance of both faces is set to 0.8 with a diffuse reflectivity of 0.2 (no specularity). The reference solution is the one obtained with ESARAD with a high number of rays (10^8).

Figure 7 compares the convergence of the different surface sampling strategies in function of the total number of rays and for different number of origins (with local isocell direction sampling). Each curve is obtained by averaging the results over 500 runs. For any number of origins, random spatial sampling gives poorer results than Halton sampling. Halton sampling exhibits better results than ESARAD for sufficiently large number of origins. If the number of origins is above 100, the convergence rate is higher and the error is lower than ESARAD as it was for the pointwise view factor. Above a certain threshold, if the number of origins keeps on increasing, the initial error starts increasing as well because the number of directions is not sufficient anymore. Too few origins leads to scarce spatial sampling and too many origins leads to scarce direction sampling. Uniform sampling is very similar to Halton sampling. The Gauss sampling strategy gives the best results for low number of origins thanks to the Gauss-Legendre quadrature weighting of each origin. Now that the saturation effect due to too few origins is overcome by Gauss-Legendre weighting, the effect of having too many origins leading to scarce direction sampling is clearly observed.

For 500 origins, the Gauss, uniform and Halton sampling strategies are almost equivalent and are all better than ESARAD. For instance, to get 0.2% accuracy on the REF, all three sampling strategies require almost 10 times less rays than ESARAD. For low number of origins, the Gauss sampling strategy presents even higher gain: almost 15 times less rays required to get 0.5% accuracy (with 10 origins) and this gain is increasing if the required accuracy is lower (30 for 0.2%) since the convergence rate is higher. The convergence rate τ defined in Eq. 7 ranges between 0.68 and 0.72 for the Gauss sampling and is 0.7 for the uniform sampling with 500 origins.

While still superior to ESARAD ($\tau = 0.5$), the convergence rate is lower than in the pointwise view factor case. This is due first to the multiple diffuse reflections for which directions are randomly generated and second to the isocell distribution that is fragmented among the origins.

Figure 9 shows the results obtained with Gauss spatial sampling combined with Halton direction sampling. Halton direction sampling gives slightly better results and shifts down all the curves.

Compared to isocell directions sampling, the error drops down from 0.46% to 0.39% for 10 origins and 10^4 rays and from 0.019% to 0.015% for 10^6 rays.

As introduced above, instead of generating a local set of directions at each origin, the idea of generating a global set of directions to be distributed among the origins is tested. Figure 8 compares two ways of distributing the global set of directions among the origins (Gauss spatial sampling). First, the left plot shows the results when the different directions are distributed randomly among the origins. On the right, the isocell unit disc sampling method is slightly modified so that each cell is subdivided into N_o equal sub-cells within which the ray is randomly generated. This method ensures that each origins gets a representative subset of the global directions set.

There are therefore N_{rays}/N_o cells with N_o subcells. Random attribution (Figure 8, left plot) does not give good results because the direction uniformity given by the isocell stratified sampling is broken up. The isocell sub-stratification sampling on the right plot gives better results than random distribution among the origins but slightly worse compared to the local direction sampling.

Choosing the right number of origins is geometry dependent: the higher the distance ratio (distance between elements / size of the element), the more important the surface sampling. As the distance between the surfaces increases (REF decreases), direction sampling becomes more important than the surface sampling. This is in line with a accuracy control methods usually employed in ray-tracing requiring a higher number of rays to achieved the same confidence level with a given uncertainty for lower REF (lower distance ratio) [16, 30]. Having a robust strategy independent of the number of origins (or ratio between the number of directions and origins) would be interesting.

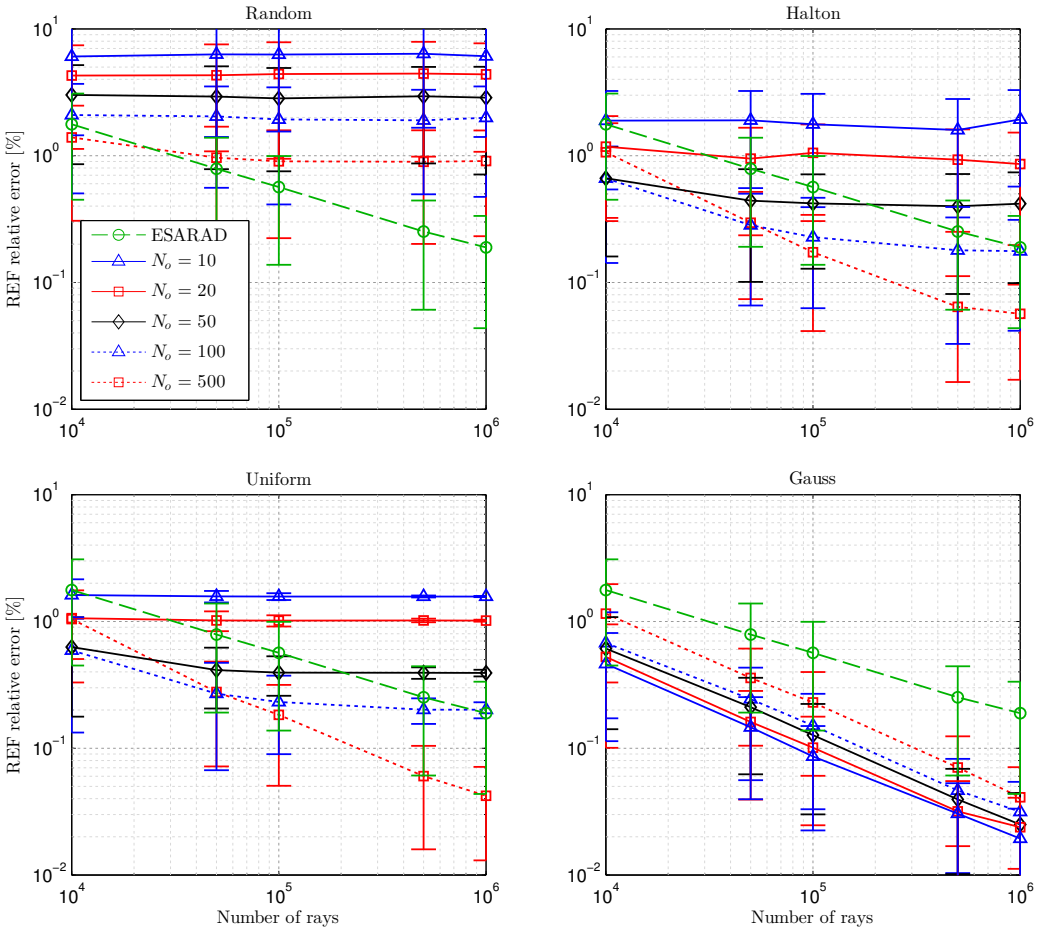

Figure 7 Relative error on the REF between the two quadrangles of Figure 6 for different surface sampling strategies and number of origins with the isocell direction sampling. Error bars give the average and corresponding standard deviation based on 500 runs.

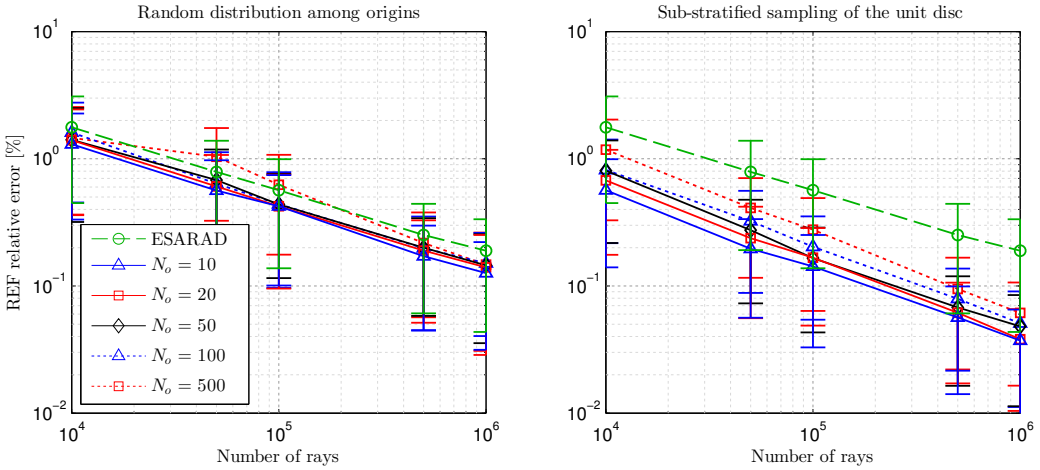

Figure 8 Relative error on the REF between the two quadrangles of Figure 6 for isocell global direction sampling and Gauss spatial sampling. On the left, the directions are distributed randomly among the origins. On the right, sub-stratification of the unit disc is performed. Error bars for 500 runs.

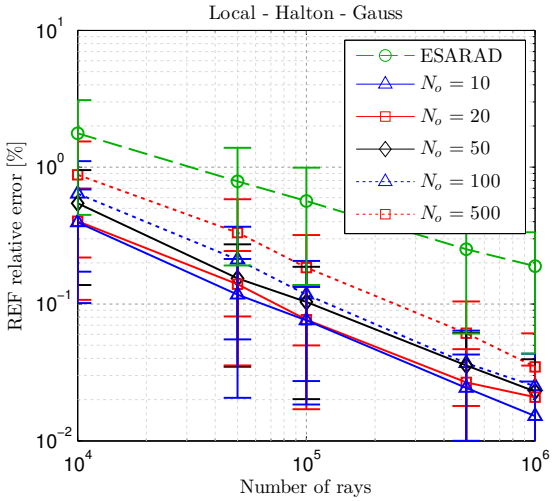

Figure 9 Relative error on the REF between the two quadrangles of Figure 6 for Halton direction sampling and Gauss spatial sampling. Error bars for 500 runs

Figure 10 shows the results obtained if each rays has its own origin ($N_{d/o} = 1$). The rays directions are randomly distributed among the same number of origins. Different combination are tested: isocell direction sampling + Random surface sampling, isocell direction sampling + Halton surface sampling and Halton for both direction and surface sampling. All three strategies give very similar results, better than ESARAD but not as good as local direction sampling with Gauss origins sampling. The convergence rate drops down to the ESARAD one ($\tau = 0.5$) and the curves are almost parallel. The gain in terms of number of rays required to achieve a given accuracy reduces to approximately 2

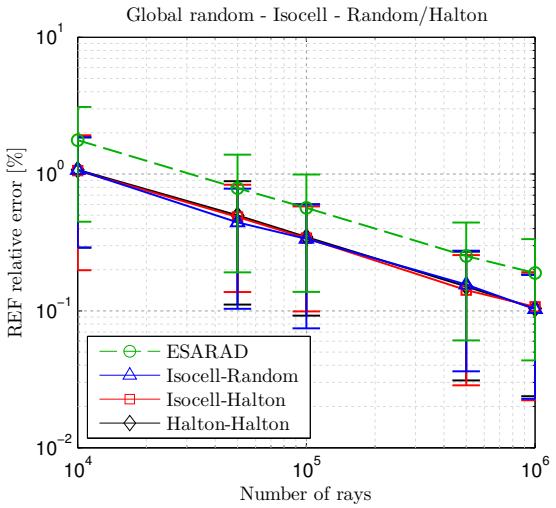

Figure 10 Relative error on the REF between the two quadrangles of Figure 6 for global direction with the same number of rays as origins. The different combination of direction and surface sampling schemes give similar results, all better than ESARAD. Error bars for 500 runs

instead of 10 or higher with local sampling. There is therefore a trade-off to be made between having a parameter (number of origins) difficult to choose and geometry dependent but potentially giving much better results and removing this parameter at the cost of a loss of accuracy but still better than conventional technique.

EUI INSTRUMENT ENTRANCE BAFFLE

So far only two faces (elements) were considered. In this section, the new method is applied to a real structure with multiple faces.

The EUI instrument

The Extreme UV Imager instrument (later referred to EUI) is a remote sensing space instrument currently under development at the Centre Spatial de Liège (CSL) [31] in Belgium. It was selected to fly on-board the Solar Orbiter Mission (Figure 11-(a)), the first European Space Agency medium-class mission (from ESA's Cosmic Vision 2015-2025 Programme) dedicated to study the solar and heliospheric physics. The spacecraft will be launched in an Sun-centered orbit with a perihelion as close as 0.28 A.U. (Astronomical Unit). The solar heat flux increasing quadratically as the distance to the Sun decreases, it will reach 13 solar constant (17500 $[\mathrm{W/m^2}]$) at perihelion. The thermal design of the instrument is therefore very critical and the temperature within the instrument ranges from 150°C to -50°C. Highly reflective baffles are located at the entrance of the two high resolution imagers. The entrance baffles are made of CFRP (carbon-fiber-reinforced plastics) with high thermal conductivity carbon fibers. They are internally coated with an Aluminum coating also developed at CSL to provide high solar specular reflectivity. Their conical shape is designed to reflect the unwanted solar flux and protect the entrance filters that are located at the end of the baffles. The extreme UV entrance filter is particularly critical because it is made of a 150 [nm] thick Aluminum foil. A dual heat pipe system is connected to a thermal interface provided by the spacecraft to remove the heat absorbed by the entrance baffles and filters to avoid overheating. The instrument is depicted in Figure 11-(b). EUI entrance baffle is an ideal example to test the new method.

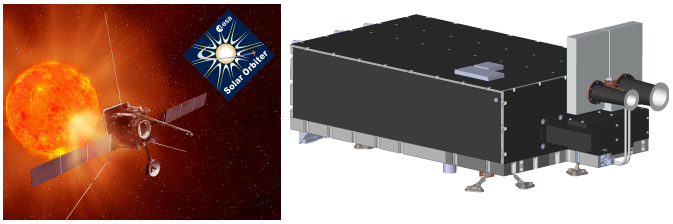

(a) (b)

Figure 11 (a) Solar Orbiter spacecraft, artist rendering, Courtesy of ESA & Astrium UK. (b) EUI instrument CAD model. The entrance baffle of the three channels are located on the right

Comparison metrics

So far, only one exchange factor was compared with its reference value. For more complicated models with many REFs, it is prohibitive to compare the REF one by one. Global comparison metrics must be used and are defined here below.

As done in [32], the RMS (root-mean-square) error is used as comparison metrics for the whole REF matrix. Again, the reference solution is the ESARAD solution obtained with an sufficiently large number of rays. The reference REFs are noted B_{ij}^{∞}. The absolute and relative RMS error are used.

$$\Delta_B = \sqrt{\frac{1}{N_f^2}\sum_i\sum_j (B_{ij} - B_{ij}^{\infty})^2} \tag{9}$$

As the final results are not the REFs but the temperatures, the accuracy of the method is also assessed by comparing the temperatures based on a pure radiative equilibrium (neither conduction nor convection). The temperatures are calculated based on the thermal lumped parameter formalism for its simplicity. In the case of pure radiative, steady-state heat transfer, the equation becomes linear in terms of T^4 and can be solved through matrix algebra. Once the nodal temperatures are computed, the RMS value of the errors is taken as comparison metric:

$$\Delta_T = \sqrt{\frac{1}{N_f}\sum_i (T_i - T_i^{\infty})^2} \tag{10}$$

Results

Figure 12 shows the mesh that is composed of 363 vertices and 360 two-sided shells (*i.e.* 720 faces). The same 0.8 emittance is set on both sides. The average face area is 62.8 [mm^2] (ranging from 19 [mm^2] to 151 [mm^2]) and the average aspect ratio is 1.2 (ranging from 0.2 to 4.8). Although the faces have different areas, the same number of rays is fired from each face. When faces with very different area are present in the model, constant ray density (ray/m^2) might be preferred. Figure 13 presents the reference case temperature. The boundary conditions are a 3K radiative environment and a conductive interface maintaining the end of the baffle at 293K.

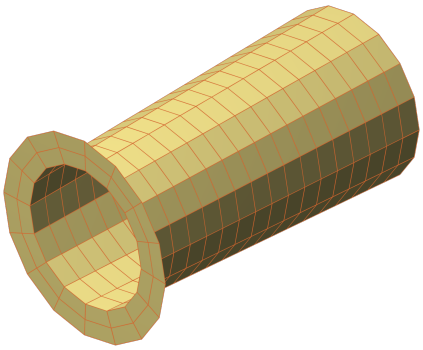

Figure 12 EUI Extreme-UV channel entrance baffle mesh

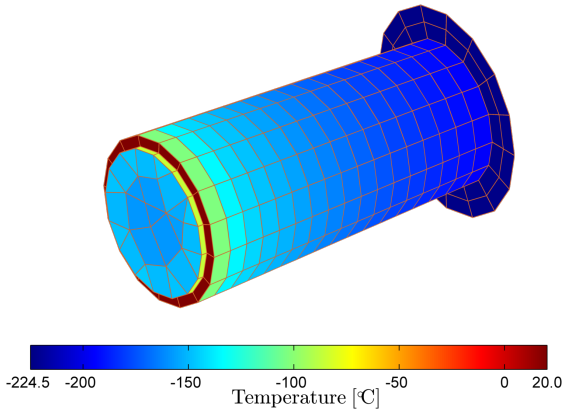

Figure 13 Temperature map for the reference radiative case. The back of the baffle is set to 20°C and the baffle is in radiative equilibrium with deep space at 3K

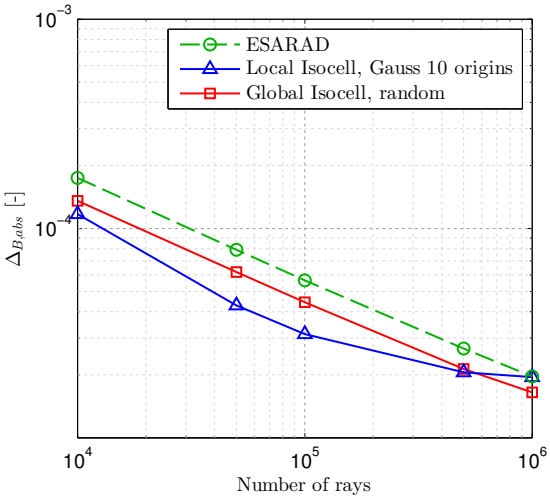

(a)

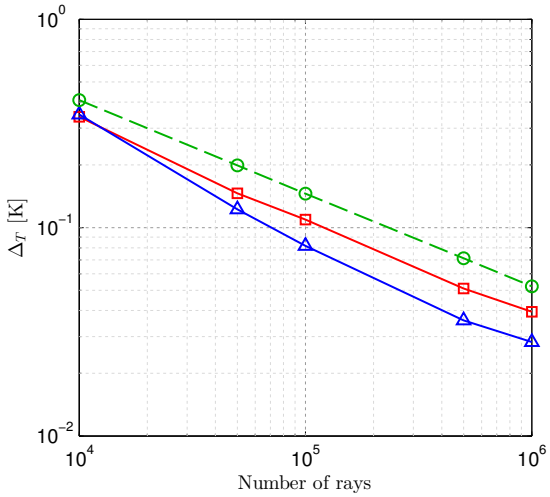

(b)

Figure 14 Convergence of the REF (left) and temperatures (right) RMS error for gauss local and random global strategies

Figure 14 shows a summary of the main strategies. It compares the local isocell direction sampling associated with 10 Gauss origins and the global isocell direction sampling with one ray per random origin to ESARAD. The comparison is based on both REF (left) and temperature (right) metrics.

Saturation of the Gauss spatial sampling is clearly visible with the REF metric but this effect is smoothed when looking at the temperatures. It confirms that the number of origins is still driving the results with an optimum that is configuration dependent. On the other hand, using the isocell direction sampling with one ray per origin is more robust and still presents better results than ESARAD without any additional user input. The temperature accuracy gain of the global isocell direction sampling scheme with one ray per origin again approaches a factor 2 meaning that 50% less rays are required to achieve the same level of accuracy.

CONCLUSIONS

In this paper, the isocell method to enhance ray tracing for radiative heat transfer analysis was presented. The isocell method gives more uniform direction sampling and leads to a better convergence rate and accuracy. It has been combined with different spatial sampling schemes of the emitting surface. The choice of the spatial sampling of the emitting surface is critical. Gauss spatial sampling gives the best results but the accuracy depends on the number of origins which is geometry dependent. To overcome this parameter, a global direction sampling scheme was implemented, firing one ray per origin. While it gives slightly worse results than Gauss spatial sampling with local direction sampling, it still presents a reduction of the number of rays by a factor 2 compared to the European Space Agency thermal analysis ray tracing engine ESARAD. The method was further benchmarked in the case of a real space structure in terms of both radiative exchange factors and temperatures. The same enhancements as in the 2-faces case was observed with 50% reduction of rays.

Acknowledgements

This work is supported by the Belgian National Fund for Scientific Research (F.R.S.-FNRS) through a F.R.I.A. grant.

References

[1] Panczak, T. D., "The failure of finite element codes for spacecraft thermal analysis," *International Conference On Environmental Systems*, SAE International, Monterey, CA, USA, Jul. 1996. (Quoted page 1.)

[2] Gilmore, D., *Spacecraft Thermal Control Handbook: Fundamental Technologies*, 2nd Edition, Aerospace Press, December 2002. (Quoted pages 1 and 2.)

[3] Chin, J. H., Panczak, T. D., and Fried, L., "Spacecraft thermal modelling," *International Journal for Numerical Methods in Engineering*, 35(4), pp. 641–653, Sep. 1992.

[4] Panczak, T. D., Ring, S., and Welch, M., "True concurrent thermal engineering integrating CAD model building with finite element and finite difference methods," *9th Thermal and Fluids Analysis Workshop Proceedings*, NASA Glenn Research Center, Cleveland Ohio, pp. 217–232, Sep. 1998. (Quoted page 1.)

[5] Panczak, T. D. and Welch, M., "Integrating thermal and structural analysis with thermal desktop™," *SAE*, 01, pp. 2126, (1999).

[6] Cullimore, B., Panczak, T. D., Baumann, J., Genberg, V., and Kahan, M., "Integrated analysis of thermal/structural/optical systems," *SAE*, 1, pp. 2444, (2002). (Quoted page 1.)

[7] Howell, J. R., "The monte carlo method in radiative heat transfer," *Transactions - American Society Of Mechanical Engineers Journal Of Heat Transfer*, 120 (3), pp. 547–560, (1998). (Quoted page 1.)

[8] Howell, J. R., Siegel, R., and Mengüç, M. P., *Thermal radiation heat transfer*, 5th Edition, CRC Press, Boca Raton, Fla., Sep. 2010.

[9] Modest, M. F., *Radiative heat transfer*, 3rd Edition, Academic Press, Amsterdam ; Boston, (2013). (Quoted pages 1, 2, and 4.)

[10] Fleck, J. J., "The calculation of nonlinear radiation transport by a monte carlo method.," , Tech. Rep. UCRL–6698(Del.), 4466389, Lawrence Radiation Lab., Univ. of California, Livermore, Livermore, Jan. 1961. (Quoted page 2.)

[11] Howell, J. R. and Perlmutter, M., "Monte carlo solution of thermal transfer through radiant media between gray walls," *Journal of Heat Transfer*, 86(1), pp. 116, (1964). (Quoted page 2.)

[12] Howell, J. R., (1968). "Application of monte carlo to heat transfer problems," . *Advances in Heat Transfer*. Vol. 5. Elsevier, pp. 1–54. (Quoted page 2.)

[13] Owen, A. B., "Quasi-monte carlo sampling," *Monte Carlo Ray Tracing: Siggraph*, 1, pp. 69–88, (2003). (Quoted pages 2 and 3.)

[14] Glassner, A. S. (Ed.), *An introduction to ray tracing*, Academic Press Ltd., London, UK, UK, (1989).

[15] Koeck, C., Coffinier, P., Auberger, X., and Rebis, J.-J., "Kernel algorithms document - ESARAD," , Tech. rep., ESA ESTEC; MATRA/ERC, (1994). (Quoted pages 2 and 4.)

[16] Planas Almazan, P., "Accuracy of monte carlo ray-tracing thermal radiation calculations: A practical discussion," *EUROPEAN SPACE AGENCY -PUBLICATIONS- ESA SP-400*, European Space Agency, Noordwijk, The Netherlands, pp. 579–591, May 1997. (Quoted pages 2 and 5.)

[17] Lambert, J. H., *Photometria, sive, De mensura et gradibus luminis, colorum et umbrae (On the Measure and Gradations of Light, Colors, and Shade)*, V.E. Klett, Augustae Vindelicorum, (1760). (Quoted page 2.)

[18] Nusselt, W., "Graphische bestimmung des winkelverhaltnisses bei der wärmestrahlung," *Zeitschrift des Vereines Deutscher Ingenieure*, 72(20), pp. 673, (1928). (Quoted page 3.)

[19] Malley, T. J., A Shading Method for Computer Generated images, Master's thesis, University of Utah, (1988). (Quoted page 3.)

[20] Cohen, M. F. and Greenberg, D. P., "The hemi-cube: A radiosity solution for complex environments," *SIGGRAPH Comput. Graph.*, 19(3), pp. 31–40, Jul. 1985. (Quoted page 3.)

[21] Vueghs, P., Innovative Ray Tracing Algorithms for Space Thermal Analysis, PhD thesis, University of Liège, 03 2009. (Quoted page 3.)

[22] Lemieux, C., *Monte Carlo and Quasi-Monte-Carlo Sampling*, Springer, (2009). (Quoted page 3.)

[23] Cumber, P. S., "Accelerating ray convergence in incident heat flux calculations using Sobol sequences," *International Journal of Thermal Sciences*, 48(7), pp. 1338–1347, (2009). (Quoted page 3.)

[24] Halton, J. H., "Algorithm 247: Radical-inverse quasi-random point sequence," *Communications of the ACM*, 7(12), pp. 701–702, Dec. 1964. (Quoted page 3.)

[25] Arvo, J., Hanrahan, P., Jensen, H. W., Mitchell, D., Pharr, M., Shirley, P., , and Fajardo, M., *State of the Art in Monte Carlo Ray Tracing for Realistic Image Synthesis*, ACM SIGGRAPH 2001 course 29 Edition, ACM Press, New York, (2001). (Quoted page 3.)

[26] Masset, L., Brüls, O., and Kerschen, G., "Partition of the circle in cells of equal area and shape," , Tech. rep., University of Liège, (2012). (Quoted pages 3 and 4.)

[27] Beckers, B. and Beckers, P., "A general rule for disk and hemisphere partition into equal-area cells," *Computational Geometry*, 45(7), pp. 275–283, Aug. 2012. (Quoted page 3.)

[28] Cook, R. L., "Stochastic sampling in computer graphics," *ACM Transactions on Graphics*, 5(1), pp. 51–72, Jan. 1986. (Quoted page 3.)

[29] ESARAD™ User Manual - UM-ESARAD-024, oct 2007. Alstom Aerospace, Cambridge Road, Whetstone, Leicester LE8 6LH United Kingdom. (Quoted page 4.)

[30] Almazan, P. P., "Statistical error control for radiative software based on monte carlo methods," , Tech. Rep. 932258, SAE International, Warrendale, PA, Jul. 1993. (Quoted page 5.)

[31] Halain, J.-P., Rochus, P., Appourchaux, T., Berghmans, D., Harra, L., Schühle, U., Auchère, F., Zhukov, A., Renotte, E., Defise, J.-M., Rossi, L., Fleury-Frenette, K., Jacques, L., Hochedez, J.-F., and Ben Moussa, A., "The technical challenges of the solar-orbiter EUI instrument," *Proceedings of the SPIE*, Vol. 7732, Jul. 2010. (Quoted page 7.)

[32] Zeeb, C. N., Performance and accuracy enhancements of radiative heat transfer modeling via Monte Carlo, PhD thesis, Colorado State University, (2002). (Quoted page 8.)